A Convex Optimization Approach for Task-Invariant Control of Modular, Lower-Limb Exoskeletons

Jianping Lin, *Member, IEEE*, Nikhil V. Divekar, *Student Member, IEEE*, Vamsi Peddinti, Gray C. Thomas, *Member, IEEE*, Robert D. Gregg, *Senior Member, IEEE*

Abstract—**Backdrivable, lower-limb exoskeletons have the potential to assist volitional motions of able-bodied users and people with mild to moderate gait disorders. Devices like the modular, backdrivable, lower-limb unloading exoskeleton (*M-BLUE*) have demonstrated the mechanical capabilities necessary to assist these activities in restricted contexts. However, a control framework does not currently exist that can be deployed on any joint and assist any activity of daily life in a provably stable manner. Our previous energy-shaping controller was optimally task-invariant but not adjustable, modular, or distributed to handle different joint configurations, and it relied on a hard stance-swing switching behavior that was outside the scope of the stability analysis. This paper presents the modular, multi-task optimal energy shaping (*M-TOES*) framework for designing controllers for any lower-limb joint configuration, using a convex formulation of the multi-task optimization problem. The framework is adjustable, distributed, and smoothly transitions between stance and swing within the scope of the stability analysis. We validate different joint configurations of the controller on N=8 able-bodied participants ambulating over a multi-activity course including sit-stand, walking on level ground and ramps, and stair ascent/descent.**

Index Terms—**Partial assistance, backdrivability, task-invariant, torque control.**

I. INTRODUCTION

EXOSKELETONS on the market today in rehabilitation applications, such as the ReWalk Personal [1], the Ekso Bionics Indego [2], and Wandercraft's Atalante X [3], are known for having actuators that provide large output torques and permit complete assistance to track pre-defined reference trajectories, as appropriate for severe impairments like paraplegia. However, these design decisions limit their applicability. Despite their promising results in gait rehabilitation, such powerful actuators introduce high mechanical impedance at the joint, which impedes backdriving of the joint (the human's ability to move the device under their own power). Similarly, kinematic control methods replicate the normative joint kinematics associated with one specific task and user at a time [4], but cannot adjust to continuously varying tasks. As a result, users of these systems cannot voluntarily move their joints and

are typically forced to follow the pre-defined joint movement patterns. Thus, the traditional exoskeleton configuration and assistance scheme is not appropriate for people with remnant voluntary ability.

Backdrivable exoskeletons, by contrast, are ideal for populations with remnant voluntary ability. Low-impedance actuation systems, such as quasi-direct-drive (QDD) actuators [5]–[9] and series elastic actuators (SEAs) [10]–[13], have enabled a recent paradigm shift from task-specific, kinematic-tracking to task-invariant, torque-tracking approaches that deliver *partial* rather than *complete* assistance to the user. Backdrivable designs allow augmentation of voluntary human motion [8], [14], compensation for human-exoskeleton mass/inertia [15], [16], and direct amplification of human strength [17]. Our group's recently developed accessible hardware platform, the modular backdrivable lower-limb unloading exoskeleton (*M-BLUE*) [18] used in this paper, exemplifies the field's trend toward lighter, minimalist structures for attaching QDD actuators to people. However, while backdrivable exoskeletons may be mechanically close to integrating into every-day life, their control systems are not up to this challenge yet. More general exoskeletons systems (such as M-BLUE) would need a controller that operates reliably across all the core activities of daily life, allows for adjustment of the control behavior, avoids instability, and handles the wide diversity of possible configurations of actuators, sensors, and (potentially distributed) embedded computers.

Recently, a diverse set of controllers have emerged for multi-task assistance using backdrivable exoskeletons, including black-box deep learning [19], state-estimation [], nonlinear adaptive oscillators [], and classification-based multi-controller switching systems []. However, these controllers do not attempt to analyze the stability of the exoskeleton–operator interaction, leaving them at risk of ...

Energy shaping [20], [21] is a nonlinear control approach based on classical dynamics that designs controllers to reshape the open-loop plant to have a new Lagrangian (or, equivalently, Hamiltonian) energy function when the loop is closed. Considering the human-exoskeleton system as the plant, energy-shaping control has previously enabled task-invariant assistance in a backdrivable knee-ankle exoskeleton [5], [22], [23]. However, underactuated systems like exoskeletons or biped walkers can only achieve closed-loop dynamics that satisfy a set of nonlinear partial differential equations called the *matching conditions*. Our previous work on energy-shaping

The authors were with the Departments of Robotics (N.V.D., G.C.T., R.D.G.) and Electrical and Computer Engineering (J.L., V.P.), University of Michigan, Ann Arbor, MI 48109, USA. (Correspondence: rdgregg@umich.edu)

control has advanced solutions to the matching conditions for exoskeletons of increasing complexity, starting from a unilateral ankle-only system [24], and advancing through a unilateral ankle-knee system in several stages: first handling known [22] or unknown [25] ground-contact conditions, then adding passive velocity feedback [23], ground reaction force feedback [26], and global angle information [27]. Each additional feature necessitated a restructuring of the matching condition rules and a new parameterization of target energies that allowed these conditions to be satisfied. Currently, a port-Hamiltonian representation of the dynamics of the human and exoskeleton can be reshaped according to the theory of interconnection and damping assignment passivity-based control (IDA-PBC) [28], [29]. However, with such abstract and complicated system descriptions, it is not practical to design the target energy by hand. While potential-energy-shaping systems can be designed intuitively, for example by using virtual model control [30], more complex energy targets have proven better suited to being optimized to produce task-invariant assistance [23], [27], [31].

Thus, a more general formulation of the energy shaping controller is needed to allow deployment on general exoskeleton systems, and this framework should be based on optimization over possible energy shapes. In particular, the latest energy-shaping controller architecture in [27] cannot be implemented on several common exoskeleton configurations (that can be achieved with M-BLUE), including unilateral and bilateral hip, and unilateral and bilateral knee configurations. These specific limitations are due to a matching conditions solution unique to exoskeleton configurations that are the beginning or end of a kinematic chain. In addition, the controller was designed to switch discretely when contact with the ground is detected, which makes it difficult to handle the multi-contact scenarios in bilateral exoskeleton configurations. Other limitations include a fully centralized controller (incompatible with the multi-embedded-computer setup required for bilateral M-BLUE configurations), a lack of adjustability in situations where user feedback directly contradicted the dataset's prescribed human torque, and an optimization that required generic nonlinear solvers rather than computationally efficient convex optimization.

This paper introduces and tests an improved version of the optimized energy-shaping controller framework that is appropriate for the M-BLUE modular exoskeleton system. More specifically, the contributions of this paper are summarized as follows. First, we introduce a general-purpose, modular, convex-optimization-based framework for multi-task optimized energy shaping (M-TOES). This framework extends our previous port-Hamiltonian control paradigm [27] by adding the key features of modular energy bases, convex penalties on incorrect torque sign, robust constraint enforcement, and unification of stance and swing controllers. Second we rigorously analyze the behavior of the target energy resulting from these controllers, including all possible power leaks. Third, we empirically validate the stability, modularity, and task-invariance of the resulting controllers with (N=8) able-bodied participants on an ADL-simulating test track for four different configurations of the M-BLUE system: unilateral hip,
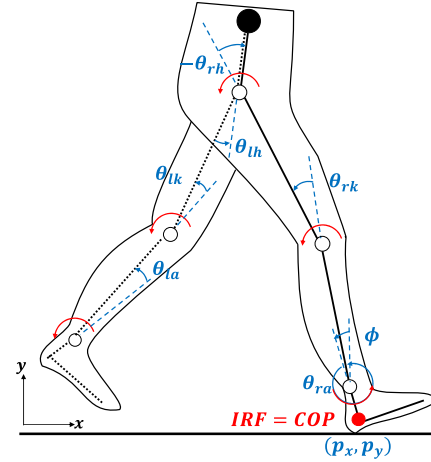

Fig. 1. Kinematic model of the human body. COP denotes the center of pressure. Solid links denote the stance leg, and dashed links denote the swing leg. Red arcs indicate torques.

bilateral hip, unilateral knee, and bilateral knee. For each modular configuration of the device, the M-TOES controller is optimized across multiple tasks (including multi-speed walking, ramps, stairs, start-stop, and sit-to-stand tasks) from an able-bodied locomotion dataset [32].

The rest of this paper is organized as follows. Section II revisits the port-Hamiltonian control framework for an under-actuated human-exoskeleton system with an arbitrary configuration of assisted joints and available sensors. We also present an updated and provably convex approach to optimizing the target energy function. Section III presents the hardware implementation and able-bodied human subject experiments. Finally, we summarize the study and provide possible future research directions.

II. ENERGY SHAPING CONTROL FOR EXOSKELETONS OF GENERAL SAGITTAL CONFIGURATIONS

This section introduces our lower-body sagittal-plane model of the human-exoskeleton system using a port-Hamiltonian formulation, and revisits interconnection and damping assignment passivity-based control (IDA-PBC). Allowing for an arbitrary configuration of assisted joints and available sensors, we present a solution to the matching conditions (considering contact constraints) and define an optimization that will efficiently produce the corresponding control law for each possible configuration.

A. Port-Controlled Hamiltonian Dynamics

We model each leg of the human-exoskeleton system as a 4-link sagittal plane monopod that starts from a floating foot and has three revolute joints (Fig. 1). During the ipsilateral heel contact phase, the inertial reference frame (IRF) is coincident with the position of the ipsilateral heel (p_{Ix}, p_{Iy}). The global heel angle ϕ_I is defined with respect to the vertical axis. The ankle, knee, and hip angles of ipsilateral (and contralateral) legs are denoted by θ_{Ia} (θ_{Ca}), θ_{Ik} (θ_{Ck}), and θ_{Ih} (θ_{Ch}), respectively. The model's masses and moments of inertia reflect the combination of the human and exoskeleton masses.

The dynamics of the ipsilateral and contralateral monopod models are linked by an interaction wrench at the hip center $F = [f_x, f_y, \tau_z]^T$ that acts equal and opposite on their respective torso bodies. The six degree-of-freedom (DOF) ipsilateral monopod model has the generalized coordinates

$$q_I = [p_{Ix}, p_{Iy}, \phi_I, \theta_{Ia}, \theta_{Ik}, \theta_{Ih}]^T \in \mathbb{R}^{6 \times 1},$$

in the 6-dimensional configuration space $\mathcal{Q}$ (Fig. 1). The conjugate momenta $p_I = M(q_I)\dot{q}_I \in \mathbb{R}^{6 \times 1}$ are defined by the positive-definite inertia matrix $M(q_I) \in \mathbb{R}^{6 \times 6}$ and the velocity vector $\dot{q}_I$. The port-controlled Hamiltonian dynamics can be characterized by the Hamiltonian $\mathcal{H}_I = \mathcal{H}(q_I, p_I) : T^*\mathcal{Q} \to \mathbb{R}$ through the equations

$$\begin{bmatrix} \dot{q}_I \\ \dot{p}_I \end{bmatrix} = \begin{bmatrix} 0_{6 \times 6} & I_{6 \times 6} \\ -I_{6 \times 6} & 0_{6 \times 6} \end{bmatrix} \nabla \mathcal{H}_I + \begin{bmatrix} 0_{6 \times 1} \\ \tau_I + A_I^T \lambda_I \end{bmatrix}, \quad (1)$$

where the skew-symmetric matrix above is known as the interconnection matrix. The Hamiltonian function $\mathcal{H}_I = \frac{1}{2} p_I^T M^{-1}(q_I) p_I + V(q_I)$ is given by the kinetic plus potential energy $V(q_I) \in \mathbb{R}$. The gradient $\nabla \mathcal{H}_I = [\partial_{q_I}\mathcal{H}_I, \partial_{p_I}\mathcal{H}_I]^T$ is a column vector in $\mathbb{R}^{12 \times 1}$ with $\partial_{q_I}\mathcal{H}_I, \partial_{p_I}\mathcal{H}_I \in \mathbb{R}^{1 \times 6}$ as row vectors. The vector of joint torques $\tau_I \in \mathbb{R}^{6 \times 1}$ aggregates the exoskeleton input $\tau_{I\text{exo}} = B_I u_I$ and the human input $\tau_{I\text{hum}} = G_I v_I + J_I^T F$ with the Jacobian matrix J_I. The control inputs $u_I \in \mathbb{R}^{m \times 1}$ and $v_I \in \mathbb{R}^{3 \times 1}$ respectively represent the exoskeleton and human torques (at the ankle, knee, and/or hip joints), which are mapped into the overall dynamics via matrices $B_I \in \mathbb{R}^{6 \times m}$ and $G_I \in \mathbb{R}^{6 \times 3}$, where m denotes the number of the exoskeleton actuators. The system is underactuated with the number of generalized coordinates larger than the number of control inputs, i.e., $6 \geq m$.

The holonomic contact constraints in the human-exoskeleton dynamics (Fig. 2) can be expressed as $a_\ell(q_I) = 0_{c \times 1}$, where c is the number of constraints for the stance leg and the subscript $\ell \in \{\text{heel}, \text{flat}, \text{toe}\}$ indicates the contact configuration. The constraint matrix $A_I = A(q_I) = \partial_{q_I} a_\ell \in \mathbb{R}^{c \times 6} = [A_\ell(q_I), 0_{c \times 3}]$ satisfies $A_I \dot{q}_I = A_I (\partial_{p_I} \mathcal{H}_I)^T = 0$ given the top row of (1). The possible cases are

$$\text{Heel Contact} \quad A_{\text{heel}}(q_I) = \begin{bmatrix} I_{2 \times 2} & 0_{2 \times 1} \end{bmatrix},$$
$$\text{Flat Foot} \quad A_{\text{flat}}(q_I) = I_{3 \times 3}, \text{ and}$$
$$\text{Toe Contact} \quad A_{\text{toe}}(q_I) = \begin{bmatrix} 1 & 0 & -l_f \sin(\phi_I) \\ 0 & 1 & l_f \cos(\phi_I) \end{bmatrix},$$

where γ is the slope angle and l_f is the length of the foot. The Lagrange multiplier $\lambda_I \in \mathbb{R}^{c \times 1}$ represents the GRFs, which are mapped into the system through the constraint matrix A_I. Details for the contact constraints are given in [5], [22]. Henceforth we omit q_I and p_I terms in matrices to simplify notation.

The Lagrange multiplier λ_I can then be obtained by solving $\frac{d}{dt}[A_I(\partial_{p_I}\mathcal{H}_I)^T] = 0 \rightarrow \partial_{q_I}[A_I(\partial_{p_I}\mathcal{H}_I)^T]\dot{q}_I + \partial_{p_I}[A_I(\partial_{p_I}\mathcal{H}_I)^T]\dot{p}_I = 0$ for

$$\lambda_I = (A_I \partial_{p_I^2}^2 \mathcal{H}_I A_I^T)^{-1} \{ -\partial_{q_I}[A_I(\partial_{p_I}\mathcal{H}_I)^T](\partial_{p_I}\mathcal{H}_I)^T$$
$$+ A_I \partial_{p_I^2}^2 \mathcal{H}_I [(\partial_{q_I}\mathcal{H}_I)^T - \tau_I] \},$$
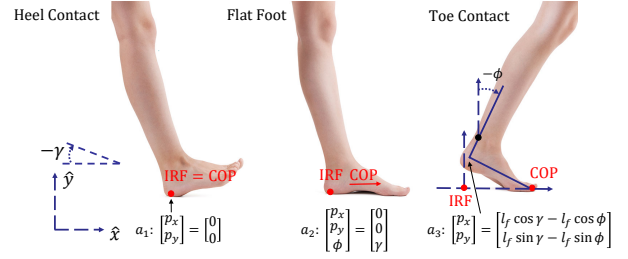

Fig. 2. Heel contact (left), flat foot (center), and toe contact (right) during the single-support period of human locomotion. Angle γ is the ground slope. This figure is updated from [5].

where $\partial_{p_I^2}^2 \mathcal{H}_I \in \mathbb{R}^{6 \times 6}$ denotes the second-order derivative of $\mathcal{H}_I$ with respect to p_I.

B. Control Law Satisfying the Matching Conditions

Assume we have closed the feedback loop for exoskeleton input u_I, while the human input v_I remains as an input to the Hamiltonian system. We consider a desired, closed-loop Hamiltonian $\tilde{\mathcal{H}}(p_I, q_I) = \frac{1}{2} p_I^T \tilde{M}_I^{-1} p_I + \tilde{V}_I$, where $\tilde{V}_I = V_I + \hat{V}_I$ represents the new potential energy with shaping term $\hat{V}_I$. The corresponding gravitational vector is $\tilde{N}_I = (\partial_{q_I}\tilde{V}_I)^T = (\partial_{q_I}V_I)^T + (\partial_{q_I}\hat{V}_I)^T = N_I + \hat{N}_I \in \mathbb{R}^{6 \times 1}$. Similar to [27], we set $\tilde{M}_I = M_I$ to simplify the matching process and passivity proof, and to avoid complicated calculations of the inertia matrix inverse in the control law, where $\nabla \tilde{\mathcal{H}}_I = \nabla \mathcal{H}_I + [\partial_{q_I}\hat{V}_I, 0]^T$. In contrast, we achieve velocity-dependent shaping by modifying the interconnection matrix of the closed-loop Hamiltonian system.

The desired closed-loop dynamics based on $\tilde{\mathcal{H}}_I$ are

$$\begin{bmatrix} \dot{q}_I \\ \dot{p}_I \end{bmatrix} = \begin{bmatrix} 0 & I \\ -I & J_{I2} \end{bmatrix} \nabla \tilde{\mathcal{H}}_I + \begin{bmatrix} 0 \\ G_I v_I + J_I^T F + A_I^T \tilde{\lambda}_I + \tilde{T}_{I\text{ex}} \end{bmatrix}, \quad (2)$$

where $\tilde{T}_{I\text{ex}} \in \mathbb{R}^{6 \times 1}$ denotes the exogenous input as in [27]. The skew-symmetric matrix $J_{I2} = -J_{I2}^T = (\partial_{q_I}Q)^T - \partial_{q_I}Q \in \mathbb{R}^{6 \times 6}$ represents the extra shaping DOF provided in the interconnection structure by the IDA-PBC method [23], where $Q(q_I) \in \mathbb{R}^{6 \times 1}$ is a smooth vector-valued function within the *artificial* gyroscopic terms $Q^T(\partial_{p_I}\mathcal{H}_I)^T$. Moreover, the closed-loop GRFs in (2) are represented by

$$\tilde{\lambda} = (A_I \partial_{p_I^2}^2 \mathcal{H}_I A_I^T)^{-1} \{ -\partial_{q_I}[A_I(\partial_{p_I}\mathcal{H}_I)^T](\partial_{p_I}\mathcal{H}_I)^T$$
$$+ A_I \partial_{p_I^2}^2 \mathcal{H}_I [(\partial_{q_I}\tilde{\mathcal{H}}_I)^T - J_{I2}(\partial_{p_I}\mathcal{H}_I)^T - G_I v_I - J_I^T F - \tilde{T}_{I\text{ex}}] \}.$$

Based on standard results in [21], Hamiltonian systems (1) and (2) *match* if we have

$$B_I u_I = -(\partial_{q_I}\tilde{\mathcal{H}}_I)^T + (\partial_{q_I}\mathcal{H}_I)^T + J_{I2}(\partial_{p_I}\mathcal{H}_I)^T$$
$$+ A_I^T(\tilde{\lambda}_I - \lambda_I) + \tilde{T}_{I\text{ex}}.$$

By plugging GRFs λ_I and $\tilde{\lambda}_I$ and following the steps in [23], we have

$$B_{I\lambda} u = X_{I\lambda}[-(\partial_{q_I}\tilde{\mathcal{H}}_I)^T + (\partial_{q_I}\mathcal{H}_I)^T + J_{I2}(\partial_{p_I}\mathcal{H}_I)^T + \tilde{T}_{I\text{ex}}], \quad (3)$$

where $X_{I\lambda} = I - A_I^T W_I A_I \partial_{p_I^2}^2 \mathcal{H}_I \in \mathbb{R}^{6\times 6}$, $W_I = (A_I \partial_{p_I^2}^2 \mathcal{H}_I A_I^T)^{-1} \in \mathbb{R}^{c\times c}$, and $B_{I\lambda} = X_{I\lambda} B_I$. The corresponding *matching condition*:

$$0 = B_{I\lambda}^\perp X_{I\lambda}[-(\partial_{q_I}\tilde{\mathcal{H}}_I)^T + (\partial_{q_I}\mathcal{H}_I)^T + J_{I2}(\partial_{p_I}\mathcal{H}_I)^T + \tilde{T}_{Iex}], \quad (4)$$

where $B_{I\lambda}^\perp \in \mathbb{R}^{(6-m)\times 6}$ is the (full-rank) left annihilator of $B_{I\lambda}$, i.e., $B_{I\lambda}^\perp B_{I\lambda} = 0$.

We can simplify the matching condition (4) by first decomposing matrix M_I into four sub-matrices as in [23]:

$$M_I = \begin{bmatrix} M_{I1} & M_{I2} \\ M_{I2}^T & M_{I4} \end{bmatrix},$$

where $M_{I1} \in \mathbb{R}^{3\times 3}$ corresponds to the floating base joints (p_{Ix}, p_{Iy}, ϕ_I) and $M_{I4} \in \mathbb{R}^{3\times 3}$ corresponds to the joints $(\theta_{Ia}, \theta_{Ik}, \theta_{Ih})$. Then we obtain

$$M_I^{-1} = \begin{bmatrix} \Delta_I^{-1} & -\Delta_I^{-1} M_{I2} M_{I4}^{-1} \\ -M_{I4}^{-1} M_{I2}^T \Delta^{-1} & M_{I4}^{-1} + M_{I4}^{-1} M_{I2}^T \Delta_I^{-1} M_{I2} M_{I4}^{-1} \end{bmatrix},$$

where $\Delta_I = M_{I1} - M_{I2} M_{I4}^{-1} M_{I2}^T \in \mathbb{R}^{3\times 3}$. As a result, we have $W_I = (A_\ell \Delta_I^{-1} A_\ell^T)^{-1}$ and $X_{I\lambda}$ can be expressed as

$$X_{I\lambda} = \begin{bmatrix} I_{3\times 3} - Z_{I\lambda} & Z_{I\lambda} M_{I2} M_{I4}^{-1} \\ 0_{3\times 3} & I_{3\times 3} \end{bmatrix},$$

where $Z_{I\lambda} = A_\ell^T W_I A_\ell \Delta_I^{-1} \in \mathbb{R}^{3\times 3}$. Let $B_I = [0, b_I^T]^T$, where $b_I \in \mathbb{R}^{3\times m}$, plug $X_{I\lambda}$ into $B_{I\lambda}$, we have $B_{I\lambda} = [b_I^T M_{I4}^{-1} M_{I2}^T Z_{I\lambda}^T, b_I^T]^T$ and the corresponding left annihilator

$$B_{I\lambda}^\perp = \begin{bmatrix} I_{3\times 3} & -Z_{I\lambda} M_{I2} M_{I4}^{-1} \\ 0_{(3-m)\times 3} & b_I^\perp \end{bmatrix},$$

where $b_I^\perp \in \mathbb{R}^{(3-m)\times 3}$ is the (full-rank) left annihilator of b_I, i.e., $b_I^\perp b_I = 0$. Plugging in $B_{I\lambda}^\perp$ and $X_{I\lambda}$ into (4), we have

$$0 = \begin{bmatrix} I_{3\times 3} - Z_{I\lambda} & 0_{3\times 3} \\ 0_{(3-m)\times 3} & b_I^\perp \end{bmatrix} [-(\partial_{q_I}\tilde{\mathcal{H}}_I)^T + (\partial_{q_I}\mathcal{H}_I)^T$$
$$+ J_{I2}(\partial_{p_I}\mathcal{H}_I)^T + \tilde{T}_{Iex}]$$
$$= \begin{bmatrix} I_{3\times 3} - Z_{I\lambda} & 0_{3\times 3} \\ 0_{(3-m)\times 3} & b_I^\perp \end{bmatrix} [-\tilde{N}_I + N_I + J_{I2} M_I^{-1} p_I + \tilde{T}_{Iex}]. \quad (5)$$

The solution (5) of the matching condition gives the feasible structure of the closed-loop system using energy shaping control.

Similarly, the six degree-of-freedom (DOF) contralateral bipedal model has the generalized coordinates

$$q_C = [p_{Cx}, p_{Cy}, \phi_C, \theta_{Ca}, \theta_{Ck}, \theta_{Ch}]^T \in \mathbb{R}^{6\times 1}.$$

The port-controlled Hamiltonian dynamics can be characterized by the Hamiltonian $\mathcal{H}_C = \mathcal{H}(q_C, p_C)$ through the equations

$$\begin{bmatrix} \dot{q}_C \\ \dot{p}_C \end{bmatrix} = \begin{bmatrix} 0_{6\times 6} & I_{6\times 6} \\ -I_{6\times 6} & 0_{6\times 6} \end{bmatrix} \nabla \mathcal{H}_C + \begin{bmatrix} 0_{6\times 1} \\ \tau_C + A_C^T \lambda_C \end{bmatrix},$$

where $\tau_C \in \mathbb{R}^{6\times 1}$ aggregates the exoskeleton input $\tau_{Cexo} = B_C u_C$ and the human input $\tau_{Chum} = G_C v_C - J_C^T F$ with the

Jacobian matrix J_C. The desired closed-loop dynamics based on $\tilde{\mathcal{H}}_C$ are

$$\begin{bmatrix} \dot{q}_C \\ \dot{p}_C \end{bmatrix} = \begin{bmatrix} 0 & I \\ -I & J_{C2} \end{bmatrix} \nabla \tilde{\mathcal{H}}_I + \begin{bmatrix} 0 \\ G_C v_C - J_C^T F + A_C^T \tilde{\lambda}_C + \tilde{T}_{Cex} \end{bmatrix},$$

with the exogenous input $\tilde{T}_{Cex} \in \mathbb{R}^{6\times 1}$.

Consider both legs together with the combined Hamiltonian $\mathcal{H} = \mathcal{H}_I + \mathcal{H}_C$, we have $q = [q_I^T, q_C^T]^T \in \mathbb{R}^{12\times 1}$ and the open-loop and closed-loop dynamics as

$$\begin{bmatrix} \dot{q} \\ \dot{p} \end{bmatrix} = \begin{bmatrix} 0_{12\times 12} & I_{12\times 12} \\ -I_{12\times 12} & 0_{12\times 12} \end{bmatrix} \nabla \mathcal{H} + \begin{bmatrix} 0_{12\times 1} \\ \tau + A^T \lambda \end{bmatrix},$$

where

$$\overbrace{\begin{bmatrix} \tau_I \\ \tau_C \end{bmatrix}}^{\tau} = \overbrace{\begin{bmatrix} B_I & 0 \\ 0 & B_C \end{bmatrix}}^{B} \overbrace{\begin{bmatrix} u_I \\ u_C \end{bmatrix}}^{u} + \overbrace{\begin{bmatrix} G_I & 0 \\ 0 & G_C \end{bmatrix}}^{G} \overbrace{\begin{bmatrix} v_I \\ v_C \end{bmatrix}}^{v} + \overbrace{\begin{bmatrix} J_I^T \\ -J_C^T \end{bmatrix}}^{J^T} F.$$

The GRFs are given by $\lambda = [\lambda_I^T, \lambda_C^T]^T \in \mathbb{R}^{2c\times 1}$ with $A^T = \begin{bmatrix} A_I^T & 0 \\ 0 & A_C^T \end{bmatrix} \in \mathbb{R}^{12\times 2c}$. The closed-loop combined dynamics based on $\tilde{\mathcal{H}} = \tilde{\mathcal{H}}_I + \tilde{\mathcal{H}}_C$ are

$$\begin{bmatrix} \dot{q} \\ \dot{p} \end{bmatrix} = \begin{bmatrix} 0 & I \\ -I & J_2 \end{bmatrix} \nabla \tilde{\mathcal{H}} + \begin{bmatrix} 0 \\ Gv + J^T F + A^T \tilde{\lambda} + \tilde{T}_{ex} \end{bmatrix}, \quad (6)$$

where $\tilde{\lambda} = [\tilde{\lambda}_I^T, \tilde{\lambda}_C^T]^T \in \mathbb{R}^{2c\times 1}$ and $\tilde{T}_{ex} = [\tilde{T}_{Iex}^T, \tilde{T}_{Cex}^T]^T \in \mathbb{R}^{12\times 1}$. The skew-symmetric interconnection structure is now $J_2 = \begin{bmatrix} J_{I2} & 0 \\ 0 & J_{C2} \end{bmatrix}$ (the quadratic form with a skew-symmetric matrix is zero). The corresponding matching conditions are given by

$$Bu = -(\partial_q \tilde{\mathcal{H}})^T + (\partial_q \mathcal{H})^T + J_2(\partial_p \mathcal{H})^T + A^T(\tilde{\lambda} - \lambda) + \tilde{T}_{ex}.$$

Plugging GRFs into the matching conditions, we have

$$B_\lambda u = X_\lambda[-(\partial_q \tilde{\mathcal{H}})^T + (\partial_q \mathcal{H})^T + J_2(\partial_p \mathcal{H})^T + \tilde{T}_{ex}], \quad (7)$$

where

$$X_\lambda = \begin{bmatrix} \overbrace{I - A_I^T W_I A_I \partial_{p_I^2}^2 \mathcal{H}_I}^{X_{I\lambda}} & 0 \\ 0 & \overbrace{I - A_C^T W_C A_C \partial_{p_C^2}^2 \mathcal{H}_C}^{X_{C\lambda}} \end{bmatrix}$$
$$= I - A^T \overbrace{\begin{bmatrix} W_I & 0 \\ 0 & W_C \end{bmatrix}}^{W} A \partial_{p^2}^2 H \in \mathbb{R}^{12\times 12},$$
$$B_\lambda = X_\lambda B = \begin{bmatrix} X_{I\lambda} B_I & 0 \\ 0 & X_{C\lambda} B_C \end{bmatrix}.$$

The corresponding *matching condition*:

$$0 = B_\lambda^\perp X_\lambda[-(\partial_q \tilde{\mathcal{H}})^T + (\partial_q \mathcal{H})^T + J_2(\partial_p \mathcal{H})^T + \tilde{T}_{ex}], \quad (8)$$

where $B_\lambda^\perp \in \mathbb{R}^{(12-2m)\times 12}$ is the (full-rank) left annihilator of B_λ, i.e., $B_\lambda^\perp B_\lambda = 0$. Following the previous matrix decomposition and simplification, we have

$$B_\lambda^\perp = \begin{bmatrix} I_{3\times 3} & -Z_{I\lambda} M_{I2} M_{I4}^{-1} & 0 & 0 \\ 0_{(3-m)\times 3} & b_I^\perp & 0 & 0 \\ 0 & 0 & I_{3\times 3} & -Z_{C\lambda} M_{C2} M_{C4}^{-1} \\ 0 & 0 & 0_{(3-m)\times 3} & b_C^\perp \end{bmatrix}.$$

Plugging in $B_\lambda^\perp$ and X_λ into (8), we have

$$0 = \begin{bmatrix} I_{3\times3} - Z_{I\lambda} & 0 & 0 & 0 \\ 0_{(3-m)\times3} & b_I^\perp & 0 & 0 \\ 0 & 0 & I_{3\times3} - Z_{C\lambda} & 0 \\ 0 & 0 & 0_{(3-m)\times3} & b_C^\perp \end{bmatrix} [-(\partial_q \tilde{\mathcal{H}})^T + (\partial_q \mathcal{H})^T$$
$$+ J_2(\partial_p \mathcal{H})^T + \tilde{T}_{\text{ex}}], \qquad (9)$$

which shows the feasible structure of the closed-loop system using energy shaping control, i.e., the shaping structure associated with the un-actuated variables. For example, considering the configuration of bilateral knees ($m = 1$), we have

$$b_I = b_C = \begin{bmatrix} 0 \\ 1 \\ 0 \end{bmatrix}, b_I^\perp = b_C^\perp = \begin{bmatrix} 1 & 0 & 0 \\ 0 & 0 & 1 \end{bmatrix}.$$

By zeroing the unactuated parts, i.e., the rows associated with $(p_{Ix}, p_{Iy}, \phi_I, \theta_{Ia}, \theta_{Ih}, p_{Cx}, p_{Cy}, \phi_C, \theta_{Ca}, \theta_{Ch})$, of $-\tilde{N} + N + J_2M^{-1}p + \tilde{T}_{\text{ex}}$, the matching condition (8) is then satisfied with the flexibility to design the skew-symmetric matrix J_2 and $\tilde{N}$.

Note that the solution (9) of the matching condition preserves the flexibility of shaping structure associated with the actuated variables, which allows us to consider the vGRF scaling, the negative power tapering strategy and the input associated with the un-actuated global variables. vGRF scaling $\mathscr{G}(\text{vGRF})$ addresses the problems with excessive torque as weight transfers from the assisted leg to the (unmodeled) contralateral leg during double support [33]. The negative power tapering strategy is included for the comfort of the subjects. Our exoskeletons can perform negative work, where the joint torques provided by the exoskeletons are opposite to the direction of joint movement. Based on the feedback from some subjects during pilot testing, negative work assistance was undesirable during certain phases of stairs descent, decline walking, and stand-to-sit transitions. Thereby, we apply a negative power tapering strategy, where the ultimate torques provided by the exoskeletons are scaled down by negative power as

$$\mathscr{F}(\tau_\theta) = \begin{cases} e^{-\beta \|\tau_\theta \cdot \dot\theta\|} \cdot \tau_\theta, & \text{if } \tau_\theta \dot\theta < 0 \\ \tau_\theta, & \text{otherwise} \end{cases} \qquad (10)$$

where $\dot\theta$ represents the joint velocity and β is the tapering coefficient.

The control law for the feasible shaping structure satisfying (7) and (9) is thus

$$Bu = [(\partial_q H)^T - (\partial_q \tilde{\mathcal{H}})^T + J_2M^{-1}p + \tilde{T}_{\text{ex}}]$$
$$u = B^+(-\hat{N} + J_2M^{-1}p + \tilde{T}_{\text{ex}})$$
$$= B^+ \cdot \mathscr{F}[\mathscr{G}(\text{vGRF}) \cdot (-\hat{N} + J_2M^{-1}p + T_{\text{ex}})], \qquad (11)$$

with $B^+ = (B^TB)^{-1}B^T$ being the left pseudoinverse of B. Note that velocity dependence is introduced via the conjugate momenta p. Moreover, we extend the exogenous input T_{ex} in [27, equation (2)] to

$$\tilde{T}_{\text{ex}} = \mathscr{F}[\mathscr{G}(\text{vGRF}) \cdot (-\hat{N} + J_2M^{-1}p + T_{\text{ex}})]$$
$$+ (\hat{N} - J_2M^{-1}p),$$

which includes the "power leak" associated with the vGRF scaling, negative power tapering, and the un-actuated global variables, adds and removes energy through a port comprising the joint torques in a way that exactly cancels the components of u that are scaled, tapered, and un-actuated. As a result, we can still satisfy matching condition (8) and use the target dynamic equation to describe the system while still incorporating the (un-actuated) global variable ϕ_I and ϕ_C into the actuated part of $\hat{N}$ and $J_2M^{-1}p$.

Given the similar structure of (6) as in [27], input-output passivity can be proved accordingly, which means that for a continuously differentiable, positive semi-definite function, the time derivative is restricted by the input times the output. Formal definition is defined in [34] as

Definition II.1. *Consider a general mechanical system*

$$\dot{x} = f(x, u), \quad y = h(x, u), \qquad (12)$$

where $x \in \mathbb{R}^{n\times1}$, $u \in \mathbb{R}^{p\times1}$ is the input and $y \in \mathbb{R}^{p\times1}$ is the output. Let $E(x): \mathbb{R}^{n\times1} \to \mathbb{R}$ be a continuously differentiable, positive semi-definite function, then the system (12) is passive from input u to output y if $\dot{E}(x) = \frac{\partial E}{\partial x} f(x, u) \le y^T u$.

Moreover, depending on the human control law, where human is assumed to modulate joint impedance [5], [35] and compensate the exogenous input $\tilde{T}_{\text{ex}}$, stability during small movements [16], [35] can be shown in the sense of Lyapunov as in [27].

C. Design Optimization

In [27], we formed multiple basis functions for the shaping terms in (11) and converted our controller design into M-TOES framework to fit weight-normalized able-bodied joint torque data for a broader set of activities. The parameters are provided by running "fmincon" with sequential quadratic programming in MATLAB. In this paper, we re-design the optimization problem to fit with "CVX [36]", which calculates the parameters more efficiently.

Similar to [27], we design $\hat{N} = -\alpha_1\xi_1 - \cdots - \alpha_i\xi_i$ and $J_2M^{-1}p = \alpha_{i+1}\xi_{i+1} + \cdots + \alpha_w\xi_w$ as linear combinations of the basis functions $\{\xi_1, \xi_2, \ldots, \xi_w\}$ with the constant coefficients $\alpha \in \mathbb{R}^{w\times1}$, where basis functions $\xi_i \in \mathbb{R}^{9\times1}$ follow the structure of (5) and w is the total number of basis functions. However, the vertical GRF (vGRF, which is normalized to one at 100% body weight) is incorporated into $\xi_i = \xi_i(q, p, \text{vGRF})$ via a sigmoid function $\mathscr{G}(\text{vGRF}) = \frac{1}{1+e^{-a\cdot(\text{vGRF}-b)}} \cdot \text{vGRF}$ for a smooth transition between the stance and swing phases. The control law (11) is thus given as

$$u = B^+(\alpha_1\xi_1 + \alpha_2\xi_2 + \cdots + \alpha_w\xi_w) = \Phi(q, p, \text{vGRF})\alpha, \quad (13)$$

where $B^+ = [0_{m\times3}, b^T b b^T]$ and $\Phi(q, p, \text{vGRF}) \in \mathbb{R}^{m\times w}$.

As mentioned in [9], an assistive torque profile provided by the exoskeletons proportional to the biomimetic torque may not be the optimal joint torque for human subjects. Moreover, based on the feedback from the subjects during the pilot testing, biomimetic torques provide knee extension during late stance, which resists the subjects lifting their legs. As a result, instead of fitting our target joint torques to the normalized

able-bodied human joint torques y_h when inputting able-bodied human kinematic trajectories as in [27], we optimize the constant coefficients α so the outputs of control law U best fit a weighted combination $Y = \Gamma_1 Y_h + \Gamma_2 Y_g + \Gamma_3 Y_0$ of the normalized able-bodied human joint torques Y_h, gravity-shaping-based joint torques Y_g, and zero (passive) joint torques Y_0, where Γ are the weighting diagonal matrices for different phases. The optimization problem is defined as

$$\text{minimize}_{\alpha, t_1, t_2, \mathbf{S}_j} \; t_1 + \Lambda_1 t_2 + \Lambda_2 \sum_j \mathbf{1}^T \mathbf{S}_j \qquad (14)$$

subject to

$$\sum_j ||U(q_j, p_j, \alpha, \text{vGRF}) - Y_j)||_2^{W_j} \le t_1, \; ||\alpha||_1^{W_s} \le t_2$$
$$-Y_j \odot U(q_j, p_j, \alpha, \text{vGRF}) \le \mathbf{S}_j, \; \mathbf{S}_j \ge 0, \quad \forall j,$$

where the subscript j represents the number of different walking tasks, including level-ground walking, ramp walking, stair climbing, and stand-to-sit. The state vectors $q_j, p_j \in \mathbb{R}^{n \times 9}$ comprise samples over time for the given task j with the number of time samples n. Vector $\mathbf{S}_j \in \mathbb{R}^{n \times 1}$ and $c = a \odot b$ denotes the pointwise product, where $c_i = a_i b_i$. The two-norm of a vector with weighting matrix W is denoted as $||\cdot||_2^W$.

The objective function comprises three parts, where scalar t_1 corresponds to the least squares error of the exoskeleton control inputs $U \in \mathbb{R}^{mn \times 1}$ and the target joint torques $Y \in \mathbb{R}^{mn \times 1}$, with the weighting diagonal matrix W_j of different tasks. Scalar t_2 represents "L1 regularization" to enforce sparsity in the model by zeroing the least important parameters in vector α, which avoids over-fitting and improves the prediction of untrained tasks as in [27]. The third part $\mathbf{1}^T \mathbf{S}_j$ (different from [27]) represents the cost of opposite signs between the exoskeleton control inputs and the target joint torques to emphasize the importance of assisting rather than resisting human torques. The term Λ weights the penalty on different costs.

We use "CVX [36]" in MATLAB to find the optimal solution α^*, where we apply the kinematic and kinetic data from nine subjects over level-ground, ramps, stairs walking [32], and stand-to-sit [37]. The vGRFs during locomotion tasks in [32], [37] are normalized by the body weight. The training tasks include level treadmill walking at $0.5, 1.5$ m/s, ascending/descending ramps with inclines of $5.2°, 11°$, ascending/descending stairs with step height of $4, 7$ inch [32], and the stand-to-sit task in [37]. The corresponding controller provides assistant torques $\tau_{\text{exo}} = \Phi(q, p, \text{vGRF})\alpha^* \cdot \text{Weight} \cdot \text{LOA}\%$, where LOA% (level-of-assistance) scales down the controller to a desired fraction of normative torque. The optimal parameters α^* are ultimately used in the real-time implementation in Section III.

III. EXPERIMENTAL VALIDATION WITH HUMAN SUBJECTS

In this section, we implement the M-TOES controller on *M-BLUE* with different configurations to partially assist multiple healthy human subjects performing multiple ADLs. The control torques and resulting muscle activation demonstrate the versatility of the proposed control approach in providing partial assistance across multiple activities.
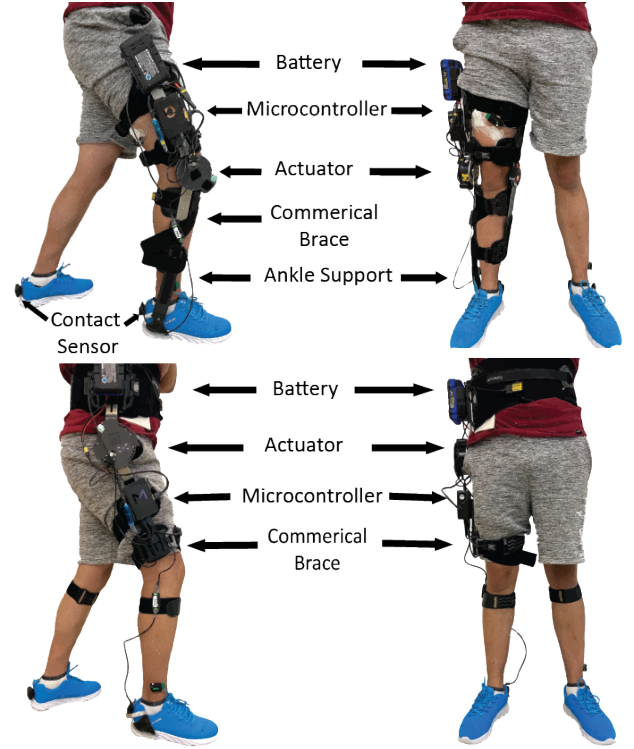

Fig. 3. *M-BLUE* hip-only and knee-only exoskeleton configurations worn by a healthy user (with an unpowered ankle brace in the knee-only configuration to support the mass of the actuator).

A. Hardware Implementation

The controller was implemented on *M-BLUE* shown in Fig. 3 (see [18] for details). The unilateral knee and hip *M-BLUE* weigh 2.36 kg and 2.15 kg (including the battery), respectively. *M-BLUE* combines the commercial off-the-shelf orthosis with a low transmission ratio of 9:1 actuator that is highly backdrivable with a static backdrive torque smaller than 0.5 Nm. The actuator can provide 9 Nm continuous torque and 18 Nm peak torque according to the manufacturer, and up to 30 Nm peak torque according to our own bench-top calibration [18]. The modular exoskeletons with the bilateral/unilateral knee and hip configurations provide flexibility to match different user requirements. The high-level control loop ran at ~ 200 Hz on a 16 GB RAM Raspberry Pi 4B for each leg, which communicated with the contralateral leg through ZeroMQ, a TCP based package. Sagittal plane joint angles, and global segment angles were provided two 6-axis Microstrain inertial measurement units. The joint angles were estimated by taking the difference between the global angles of the segments forming the joint. Compared to using actuator encoder values to estimate joint angles, this method substantially improved stability issues caused by the combined effect of the high backdrivability of M-BLUE and soft-tissue compliance. *M-BLUE* was powered by a 24 V 2 Amp-hour Kobalt battery (~ 470 g) attached to a 3D printed battery adapter mounted on the orthosis on each side. Safety features such as mechanical hard stops, thermal protectors, software program interventions, and current limiters were present at all joints.

The vGRF was measured by a commercial footwear sensor (IEE Smart Footwear [38]) placed underneath the shoe insole.
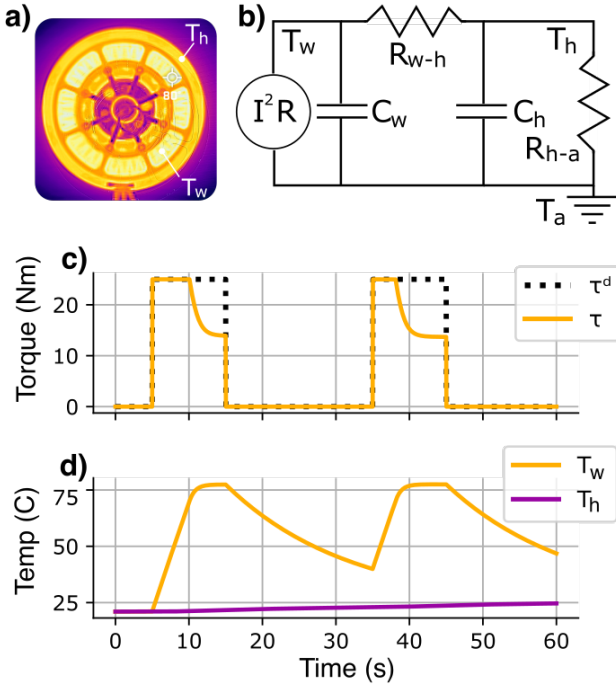
Fig. 4. **Model-based thermal limits** were identified using the dynamics of the winding temperature T_w and case temperature T_c in thermal images (a) and fit to a thermal circuit model (b), which allowed development of a safety controller that reduces desired torque (c) in order to provide strict guarantees on the maximum temperatures (d).

Similar to zero-order hold, a parallel thread was created to read vGRF continuously at ~ 55 Hz, which gave the latest vGRF every 0.02 s and avoided slowing down the main control loop at 200 Hz. The sensor was calibrated using a predefined calibration procedure before each use to achieve a final readout normalized to body weight in the same manner as the vGRFs from the normative dataset used for the controller simulation. An infinite impulse response (IIR) second-order low-pass filter (50 Hz cutoff frequency) was applied to the vGRF for noise reduction purposes. The negative power tapering coefficient β in (10) was adjusted for user comfort during several practice trials and fixed for all subjects during data collection.

B. Temperature Safety

To protect the actuators from accidental overheating, we implemented a motor current limiting controller. The controller ran a real-time simulation of the winding temperature, based on an offline system identification experiment and a simple model with two temperature states (see Fig. 4), resulting in an ODE model of the form

$$\dot{T}_w = I_q^2 R_q + \frac{T_h - T_w}{R_{w-h}C_w}, \tag{15}$$

$$\dot{T}_h = \frac{T_w - T_h}{R_{w-h}C_h} + \frac{T_a - T_h}{R_{h-a}C_h}, \tag{16}$$

where $I_q^2 R_q$ is the joule heating of the motor windings, the temperatures of the winding, housing, and ambient are denoted T_w, T_h, and T_a, respectively, and the resistive and capacitive thermal circuit elements are laid out as diagrammed in Fig. 4.b.

To ensure the temperature limits are not breached for any desired q-axis current, I_q^d, we define the true current I_q as

$$I_q = \sqrt{S_{\tilde{\sigma}_h}^{\bar{\sigma}_h}(T_h) S_{\tilde{\sigma}_w}^{\bar{\sigma}_w}(T_w)} I_q^d, \tag{17}$$

in terms of the following soft-limiting function:

$$S_{\bar{\sigma}}^{\bar{\sigma}}(T) = \begin{cases} 1 & T \leq \tilde{\sigma} \\ \frac{\bar{\sigma} - T}{\bar{\sigma} - \tilde{\sigma}} & \tilde{\sigma} < T < \bar{\sigma} \\ 0 & T \geq \bar{\sigma} \end{cases}. \tag{18}$$

This law provides the following safety guarantee while also avoiding sudden shut-offs of power to the device.

Lemma III.1. *The set of safe temperatures,*

$$\mathscr{T} = \{(T_h, T_w) \mid T_a \leq T_h \leq \bar{\sigma}_h \ T_a \leq T_w \leq \bar{\sigma}_w\},$$

is invariant under any control law that satisfies $T_w = \bar{\sigma}_w \implies I_q = 0$ (including the proposed temperature safety control law), so long as $T_a \leq \bar{\sigma}_h \leq \bar{\sigma}_w$ and $\bar{\sigma}_w - \bar{\sigma}_h \leq \frac{R_{w-h}}{R_{h-a}}(\bar{\sigma}_h - T_a)$.

Proof. Consider the four edges of this rectangular set. At the edge $T_w = T_a$, $(T_h, T_w) \in \mathscr{T}$ implies that the two terms in (15) are non-negative, so the state cannot escape $\mathscr{T}$ by passing through this edge. Similarly, at the edge $T_h = T_a$, $(T_h, T_w) \in \mathscr{T}$ implies that the first term in (16) is non-negative and the second is zero, again prohibiting escape. At the edge $T_w = \bar{\sigma}_w$, $(T_h, T_w) \in \mathscr{T}$ implies

$$\dot{T}_w\big|_{T_w=\bar{\sigma}_w} = I_q^2 R_q^{\,0} + \frac{T_h - \bar{\sigma}_w}{R_{w-h}C_w} \leq \frac{\bar{\sigma}_h - \bar{\sigma}_w}{R_{w-h}C_w} \leq 0. \tag{19}$$

And at the remaining edge $T_h = \bar{\sigma}_h$, $(T_h, T_w) \in \mathscr{T}$ implies

$$\dot{T}_h\big|_{T_h=\bar{\sigma}_h} = \frac{T_w - \bar{\sigma}_h}{R_{w-h}C_h} + \frac{T_a - \bar{\sigma}_h}{R_{h-a}C_h} \leq \frac{\bar{\sigma}_w - \bar{\sigma}_h}{R_{w-h}C_h} + \frac{T_a - \bar{\sigma}_h}{R_{h-a}C_h}$$

$$\leq \frac{\bar{\sigma}_h - T_a}{R_{w-h}C_h} + \frac{T_a - \bar{\sigma}_h}{R_{h-a}C_h} = 0. \tag{20}$$

Thus, since the state of the system cannot escape any boundary of $\mathscr{T}$, $\mathscr{T}$ is an invariant set. $\square$

In practice, this means that we can guarantee the upper winding temperature limit, $\bar{\sigma}_w$, (80 Celsius) and the upper housing temperature limit, $\bar{\sigma}_h$, (70 Celsius) are never breached without any knowledge of rest of the controller or human actions. The soft limits at $\tilde{\sigma}_w = 70$ Celsius and $\tilde{\sigma}_h = 60$ Celsius soften the loss of torque when we get to the temperature limits (Fig. 4.c-d demonstrates this behavior in simulation). Note that, in practice, the housing temperature is nearly constant in our experiments. We used a temperature sensor on the actuator module's logic board to provide an estimate for T_h, which we used in place of the simulation estimate of this value for the purposes of limiting current.

C. Human Subject Methods

The following study was approved by the Institutional Review Board at the University of Michigan (HUM00164931). We enrolled eight able-bodied human subjects (see Tab. I) to demonstrate the ability of *M-BLUE* with M-TOES to assist multiple tasks. We assessed muscle activation via EMG

TABLE I
SUBJECT DEMOGRAPHICS

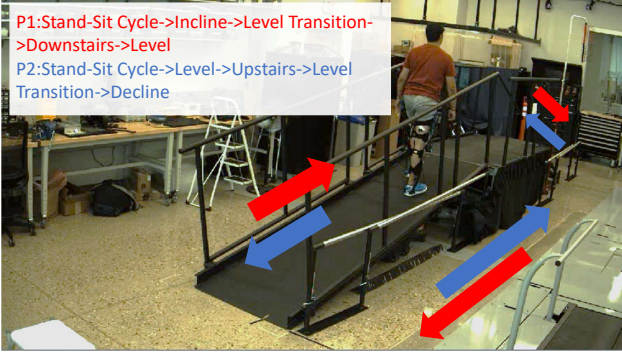| Subject	s1	s2	s3	s4	s5	s6	s7	s8
Sex	M	M	F	M	F	M	F	F
Mass (kg)	80	80	60	88	63	70	55	58

Fig. 5. S1 with bilateral knee *M-BLUE* walked on a circuit. One trial consists of Part 1 (P1) and Part 2 (P2).

(Delsys Inc.) of vastus medialis oblique (VMO), rectus femoris (RF), biceps femoris (BF), gluteus maximus (GLUT), which function as a knee extensor, knee extensor/hip flexor, knee flexor, hip extensor, respectively. We used neonatal sensors for VMO, RF, and BF. Results of bilateral knees from s2 and s3 were excluded due to failure of synchronization between left and right Raspberry Pi's, and results of BF from s4 were excluded due to failure of the sensor, which was noticed after the experiment.

The experiment comprised one trial with two parts at a self-selected speed, as shown in Fig. 5. Part 1 (P1) includes five sections: stand-sit cycle, followed by incline walking (12°), transition level walking for adjustment (on the platform), downstairs (6 inch), and level walking (on the ground). Part 2 (P2) reverses the walking direction and also includes five sections: stand-sit cycle, followed by level walking, upstairs (6 inch), transition level walking for adjustment, and decline walking (12°). All incline/decline and upstairs/downstairs sections started with the right foot contacting the ramp/stairs first to get the maximum number of strides for the right leg (not required for transition level walking and level walking). The trial (P1 and P2) was repeated for five exoskeleton modes: bare (no exoskeleton), active bilateral hip exoskeleton (HipB), active unilateral hip exoskeleton (HipU), active bilateral knee exoskeleton (KneeB), and active unilateral knee exoskeleton (KneeU). The LOA% for the active modes was set based on the subjects' comfort level during practice trials and fixed for the entire experiment. We collected 5 repetitions of each trial per exoskeleton mode. Each trial was approximately 60 seconds on average. For each subject, we collected data from a minimum of 20 gait cycles of level walking, 10 gait cycles per stairs task, 10 gait cycles per ramp task, and 10 stand-sit cycles. Subjects were instructed not to use the handrails except to prevent a fall. At least five minutes of acclimation time was provided for each mode before data collection. At least five minutes of break time between each mode was provided. A supplementary

video of the experiments is available for download.

The walking trials were separated into different tasks using a stopwatch and VICON video, and cropped into gait cycles by detecting heelstrike with a heel-mounted accelerometer. Stand-sit cycles were cropped into individual repetitions using a thigh-mounted accelerometer built into the EMG sensor. Each muscle's EMG was demeaned, bandpass filtered (20 - 200 Hz), smoothed with a moving 100 ms window RMS, and then normalized with respect to the maximum peak of the ensemble averages (across repetitions) of all the active modes [39]. This was done for each task and muscle separately, resulting in the signals being converted to a percentage of the maximum voluntary contraction level (%MVC) for consistent comparison across subjects.

D. Human Subject Results

The ensemble-averaged VMO, RF, BF, and GLUT EMGs for bare and active modes are shown in Fig. 6 for s1. In general the task-specific dominant muscles (for the stance phase) had reduced effort and peak EMG for the active modes in most tasks—VMO and RF for incline, stair ascent, and stand-sit cycle. Moreover, the assistance torque profiles matched the muscle activation profiles, explaining the reduction in muscle activation compared to bare mode.

Fig. 7 shows that even in the experiment with subject kinematics being influenced by the exoskeleton's mass and joint torque, the averaged command torques are close to the normalized able-bodied human torques from [32], [37] in certain tasks including incline walking and stairs ascent, which is measured by Cosine Similarity (SIM) with KneeB: $87.3 \pm 4.0\%$, KneeU: $79.0 \pm 11.2\%$, HipB: $86.9 \pm 4.8\%$, and HipU: $87.6 \pm 4.8\%$ for incline walking, and KneeB: $83.8 \pm 14.0\%$ and KneeU: $88.3 \pm 5.2\%$ for stairs ascent. Definition of SIM was defined in [27] and cited below

$$\text{SIM}(A,B) = \frac{100 \cdot A \cdot B}{\|A\|_2 \|B\|_2} \%.$$

Note, our target torque profile combined the normalized able-bodied human joint torques, gravity-shaping-based joint torques, and zero (passive) joint torques. We also applied the negative power tapering strategy. As a result, the objective is not to match the normalized able-bodied human torques as close as possible, which is done in [40] for torque prediction quality.

Incline walking and stairs ascent are primarily associated with positive power or concentric muscle contractions. In these tasks, the quadriceps are predominantly activated to lift the center of mass (COM) of the body. All active modes provided knee and hip extension torques in this phase, resulting in EMG reduction of the VMO and RF. Hip modules provided hip extension torques in this phase, resulting in noticeable GLUT EMG reductions compared to the bare mode for s1.

Stairs descent and decline walking are primarily associated with negative power and involve eccentric quadriceps contractions. Commonly, a double peak quadriceps activation profile is apparent in stance; firstly to absorb the impact of heel strike, and secondly to lower the COM. However, due to the negative power tapering strategy, all active modes show a minor effect
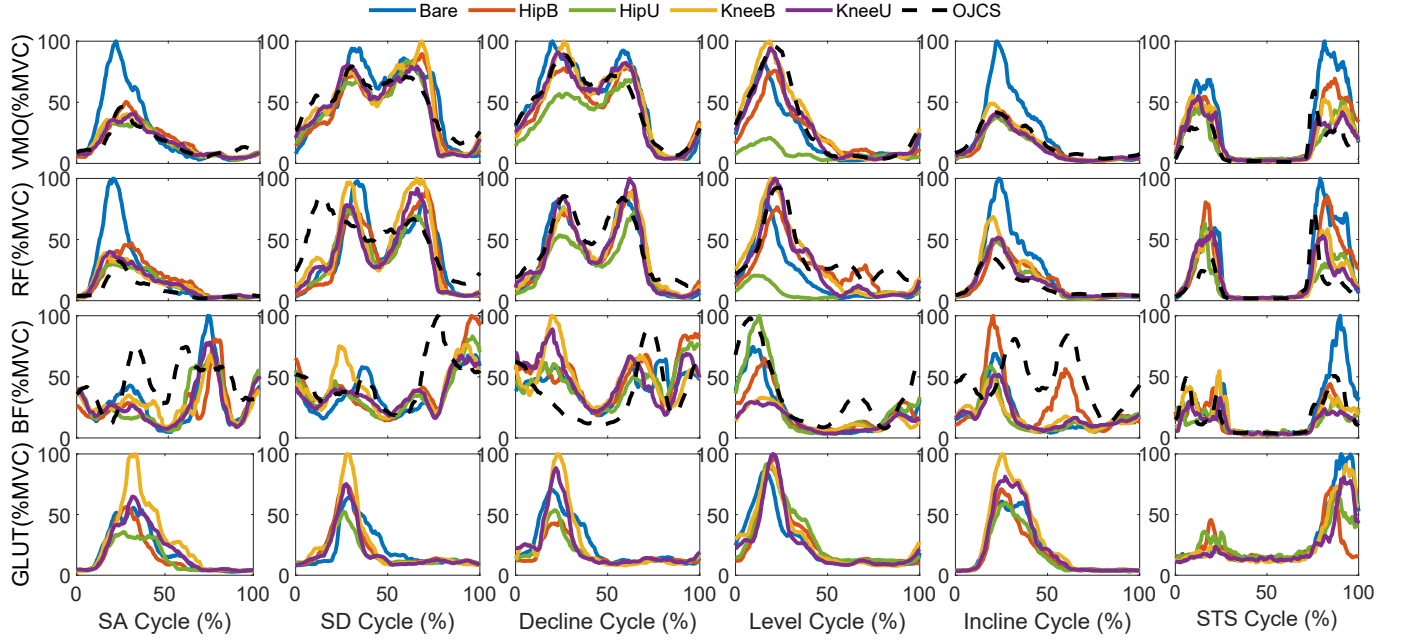
Fig. 6. Subject 1 EMG comparisons between bare and different exoskeleton configurations for each muscle (VMO, RF, BF, and GLUT) and task {Stairs Ascent/Descent (6in step height), Decline/Incline (12°), level ground, and Sit-Stand cycle}. Results are time-normalized ensemble averages across all repetitions.
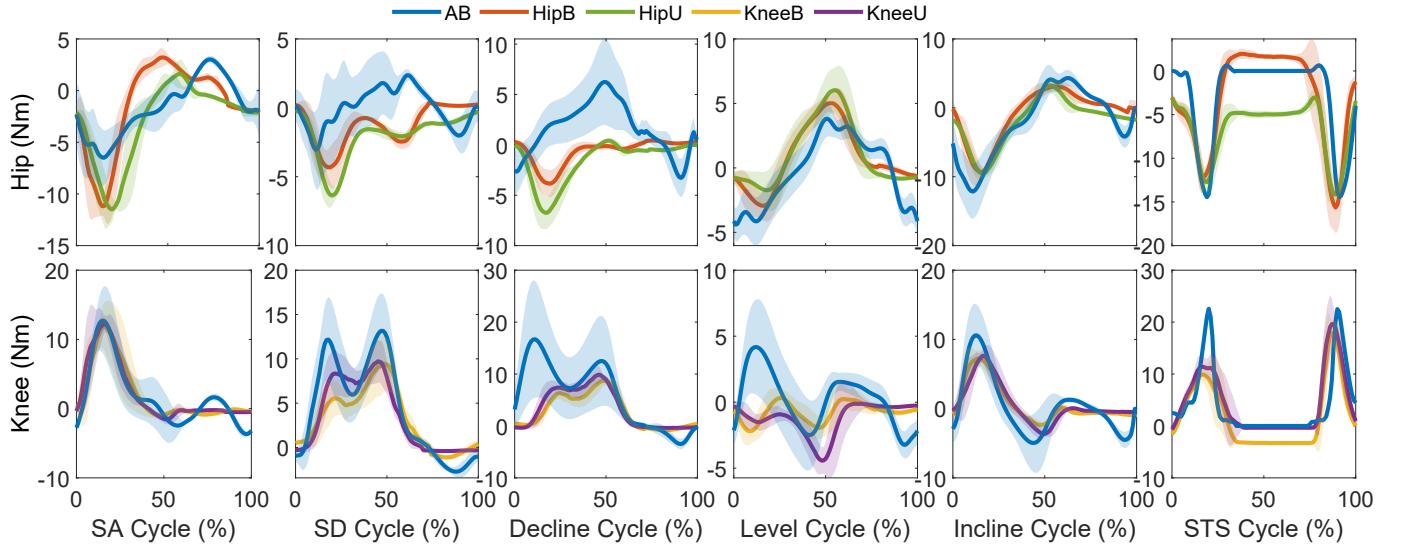

Fig. 7. Subject 1 averaged normalized command torques for experiment tasks {stair ascent/descent (6inch), decline/incline (12°), level ground, stand-sit cycle}. The red solid (HipB), the green solid (HipU) lines, the yellow solid (KneeB), and the purple solid (KneeU) lines represent the mean commanded exoskeleton torque across all repetitions for the active modes, respectively. Positive torques represent hip flexion and knee extension. Normative able-bodied (AB) human joint torques have been scaled for better comparison and illustration.

on EMG reductions compared to the bare mode. Both knee and hip modules provided minor knee and hip extension torques during early stance to absorb the impact.

Sit-to-stand and stand-to-sit primarily require knee extension torques [41]. These occur in the form of concentric contractions during sit-to-stand and eccentric contractions during stand-to-sit. All knee modules provided substantial knee extension torques, resulting in a noticeable reduction in VMO and RF (knee extensor) activations for s1.

The purpose of BF is to lift the foot by flexing the knee, aiding in leg clearance. Knee modules provided flexion torques for level walking, which resulted in BF EMG reductions compared to bare. The assistance torques provided by the hip

modules result in GLUT EMG reduction for most of the tasks. We do not see GLUT EMG reduction with knee modules since no assistance can be provided for GLUT.

We also performed a linear mixed model in MATLAB for the subject-wise muscular efforts analysis, where data from eight subjects was tabulated with information consisting of muscle effort change, controller (Bare, HipB, HipU, KneeB, KneeU), weight, LOA, and gender. Effort change is calculated by normalizing the EMG to % MVC, then calculating the integral with respect to time from the beginning to the end of five repetitive trials for each control mode to represent muscular effort as % MVC.s [33]. Lastly, we subtracted the
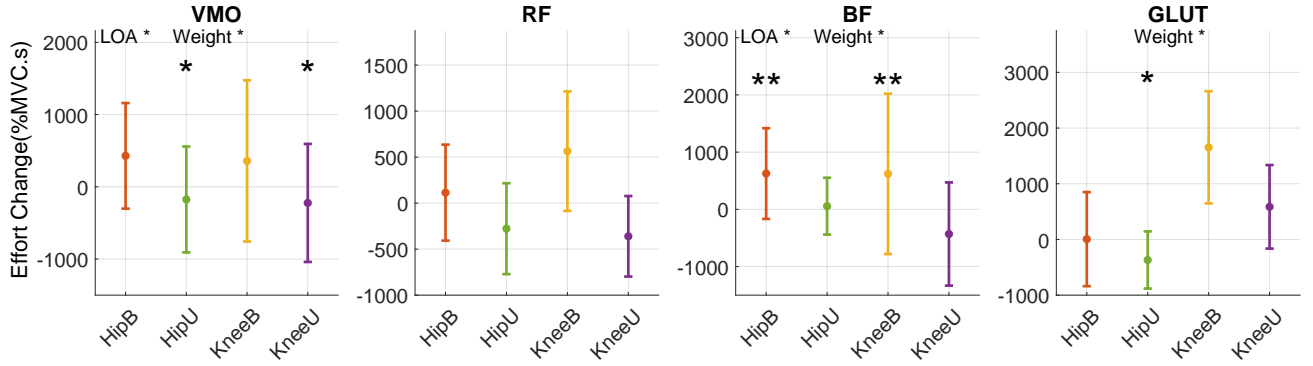
Fig. 8. Across subject comparisons of total muscle effort during five repetitions. Muscle effort is compared between the bare mode and different exoskeleton configurations for each muscle pair (VMO, RF, BF, and GLUT). A positive value represents muscle effort increment with respect to the bare mode. * represents statistical difference ($p < 0.05$). ** represents $p <= 0.01$. *** represents $p <= 0.001$.

% MVC.s of active modes by the % MVC.s of the bare mode for the effort change. We defined control modes as categorical variables and fitted a linear mixed-effects model, where the control mode, weight, LOA, and gender are the fixed effects.

The linear mixed model is given as

$$\text{Effort Change} \sim 1 + \text{Controller} + \text{LOA} + \text{Weight} + \text{Gender},$$

where 1 represents the constant term and varies by subjects, which is the expected mean value of effort change. The effort change is calculated by using the bare mode as a reference to get the relative change with respect to the active modes. Results are shown in Fig. 8, where the p-values indicate significant effects of LOA and subject weight in the effort change for VMO and BF, and significant effects of subject weight only in GLUT. There are no significant effects of gender in the effort change for all muscles. HipU and KneeU have lower muscle effort than the bare mode, with this trend being statistically significant at the significance level of 0.05 for VMO. HipU has lower muscle effort than the bare mode with this trend being statistically significant at the significance level of 0.05 for GLUT. HipB and KneeB have higher muscle effort than the bare mode, with this trend being statistically significant at the significance level of 0.01 for BF.

Among all the active modes, the hip-unilateral module shows overall the best results in EMG reduction among all tasks for s1 as shown in Fig. 6, which is not always true for all the subjects. Muscle effort reduction shows different results for each subject over various *M-BLUE* configurations, where most subjects get used to unilateral exoskeletons easily. While only subject 2,3,4 shows better reductions in muscle efforts of bilateral cases over unilateral cases. This may depend on how subjects acclimate to various configurations, where the unilateral cases are more accessible for the subjects to get adaptive. In contrast, bilateral cases add more weight and constraint due to the rigid structure of orthosis. We gave the subjects approximately 5 minutes of acclimation time for each task, whereas a prior study gave 30 minutes of acclimation time before showing EMG reductions under the assistance [42]. Thus, our outcomes could improve by providing more acclimation time.

IV. CONCLUSION

This paper investigated multi-task optimal energy-shaping (M-TOES) control for various configurations of the modular backdrivable lower-limb unloading exoskeleton (*M-BLUE*). Whereas prior work on M-TOES framework considered only the unilateral knee-ankle case, this paper generalized the framework to uni- and bi-lateral configurations of hip or knee exoskeletons, offering a re-configurable solution for different scenarios. Human trials demonstrated the potential of the implemented task-invariant M-TOES controller to reduce the muscular effort in level-ground walking, ramp ascent and descent, stair ascent and descent, and sit-stand transitions.

While this paper considered knee and hip joints separately, a combination of knee and hip exoskeletons could benefit more from M-TOES framework due to the increment in the basis functions design. Future work could also consider uni- and bi-lateral ankle, knee, and hip configurations of *M-BLUE*, for complete assistance over lower limbs.

ACKNOWLEDGMENTS

REFERENCES

[1] G. Zeilig, H. Weingarden, M. Zwecker, I. Dudkiewicz, A. Bloch, and A. Esquenazi, "Safety and tolerance of the rewalk™ exoskeleton suit for ambulation by people with complete spinal cord injury: a pilot study," *J. Spinal Cord Med.*, vol. 35, no. 2, pp. 96–101, 2012.

[2] S. A. Kolakowsky-Hayner, J. Crew, S. Moran, and A. Shah, "Safety and feasibility of using the eksotm bionic exoskeleton to aid ambulation after spinal cord injury," *J. Spine*, vol. 4, p. 003, 2013.

[3] O. Harib, A. Hereid, A. Agrawal, T. Gurriet, S. Finet, G. Boeris, A. Duburcq, M. E. Mungai, M. Masselin, A. D. Ames *et al.*, "Feedback control of an exoskeleton for paraplegics: Toward robustly stable, hands-free dynamic walking," *IEEE Control Syst. Mag.*, vol. 38, no. 6, pp. 61–87, 2018.

[4] T. Yan, M. Cempini, C. M. Oddo, and N. Vitiello, "Review of assistive strategies in powered lower-limb orthoses and exoskeletons," *Robot. Auton. Syst.*, vol. 64, pp. 120–136, 2015.

[5] G. Lv, H. Zhu, and R. D. Gregg, "On the design and control of highly backdrivable lower-limb exoskeletons: A discussion of past and ongoing work," *IEEE Control Syst. Mag.*, vol. 38, no. 6, pp. 88–113, 2018.

[6] J. Wang, X. Li, T.-H. Huang, S. Yu, Y. Li, T. Chen, A. Carriero, M. Oh-Park, and H. Su, "Comfort-centered design of a lightweight and backdrivable knee exoskeleton," *IEEE Robot. Autom. Lett.*, vol. 3, no. 4, pp. 4265–4272, 2018.

[7] H. Zhu, C. Nesler, N. Divekar, V. Peddinti, and R. Gregg, "Design principles for compact, backdrivable actuation in partial-assist powered knee orthoses," *IEEE/ASME Trans. Mechatron.*, 2021.

[8] S. Yu, T.-H. Huang, X. Yang, C. Jiao, C. Yang, Y. Chen, J. Yi, and H. Su, "Quasi-direct drive actuation for a lightweight hip exoskeleton with high backdrivability and high bandwidth," *IEEE/ASME Trans. Mechatron.*, vol. 25, no. 4, pp. 1794–1802, 2020.

[9] T.-H. Huang, S. Zhang, S. Yu, M. K. MacLean, J. Zhu, A. Di Lallo, C. Jiao, T. C. Bulea, M. Zheng, and H. Su, "Modeling and stiffness-based continuous torque control of lightweight quasi-direct-drive knee exoskeletons for versatile walking assistance," *IEEE Trans. Robot.*, 2022.

[10] F. Giovacchini, F. Vannetti, M. Fantozzi, M. Cempini, M. Cortese, A. Parri, T. Yan, D. Lefeber, and N. Vitiello, "A light-weight active orthosis for hip movement assistance," *Robotics and Autonomous Systems*, vol. 73, pp. 123–134, 2015.

[11] T. Zhang, M. Tran, and H. Huang, "Design and experimental verification of hip exoskeleton with balance capacities for walking assistance," *IEEE/ASME Transactions on mechatronics*, vol. 23, no. 1, pp. 274–285, 2018.

[12] S. V. Sarkisian, M. K. Ishmael, G. R. Hunt, and T. Lenzi, "Design, development, and validation of a self-aligning mechanism for high-torque powered knee exoskeletons," *IEEE Transactions on Medical Robotics and Bionics*, vol. 2, no. 2, pp. 248–259, 2020.

[13] I. Kang, R. R. Peterson, K. R. Herrin, A. Mazumdar, and A. J. Young, "Design and validation of a torque-controllable series elastic actuator-based hip exoskeleton for dynamic locomotion," *Journal of Mechanisms and Robotics*, vol. 15, no. 2, p. 021007, 2023.

[14] U. Nagarajan, G. Aguirre-Ollinger, and A. Goswami, "Integral admittance shaping: A unified framework for active exoskeleton control," *Robot. Auton. Syst.*, vol. 75, pp. 310–324, 2016.

[15] G. Aguirre-Ollinger, J. E. Colgate, M. A. Peshkin, and A. Goswami, "Inertia compensation control of a one-degree-of-freedom exoskeleton for lower-limb assistance: Initial experiments," *IEEE Trans. Neural Syst. Rehabil. Eng.*, vol. 20, no. 1, pp. 68–77, 2012.

[16] S. A. Murray, K. H. Ha, C. Hartigan, and M. Goldfarb, "An assistive control approach for a lower-limb exoskeleton to facilitate recovery of walking following stroke," *IEEE Trans. Neural Syst. Rehabil. Eng.*, vol. 23, no. 3, pp. 441–449, 2014.

[17] G. C. Thomas, O. Campbell, N. Nichols, N. Brissonneau, B. He, J. James, N. Paine, and L. Sentis, "Formulating and deploying strength amplification controllers for lower-body walking exoskeletons," *Front. Robot. AI*, vol. 8, p. 295, 2021.

[18] C. Nesler, G. Thomas, N. Divekar, E. J. Rouse, and R. D. Gregg, "Enhancing voluntary motion with modular, backdrivable, powered hip and knee orthoses," *IEEE Robotics and Automation Letters*, vol. 7, no. 3, pp. 6155–6162, 2022.

[19] D. D. Molinaro, I. Kang, J. Camargo, M. C. Gombolay, and A. J. Young, "Subject-independent, biological hip moment estimation during multimodal overground ambulation using deep learning," *IEEE Transactions on Medical Robotics and Bionics*, vol. 4, no. 1, pp. 219–229, 2022.

[20] A. M. Bloch, N. E. Leonard, and J. E. Marsden, "Stabilization of mechanical systems using controlled lagrangians," in *IEEE Conf. Decis. Control*, vol. 3, 1997, pp. 2356–2361.

[21] R. Ortega, A. Loría, P. J. Nicklasson, and H. J. Sira-Ramirez, *Passivity-based control of Euler-Lagrange systems*. Springer-Verlag, 1998.

[22] G. Lv and R. D. Gregg, "Underactuated potential energy shaping with contact constraints: Application to a powered knee-ankle orthosis," *IEEE Trans. Control Syst. Technol.*, vol. 26, no. 1, pp. 181–193, 2018.

[23] J. Lin, N. V. Divekar, G. Lv, and R. D. Gregg, "Optimal task-invariant energetic control for a knee-ankle exoskeleton," *IEEE Control Syst. Lett.*, 2021.

[24] G. Lv and R. D. Gregg, "Orthotic body-weight support through underactuated potential energy shaping with contact constraints," in *IEEE Conf. Decis. Control*, 2015, pp. 1483–1490.

[25] J. Lin, G. Lv, and R. D. Gregg, "Contact-invariant total energy shaping control for powered exoskeletons," in *American Control Conf.* IEEE, 2019, pp. 664–670.

[26] G. C. Thomas and R. D. Gregg, "An energy shaping exoskeleton controller for human strength amplification," in *2021 60th IEEE Conference on Decision and Control (CDC)*. IEEE, 2021, pp. 1419–1425.

[27] J. Lin, N. V. Divekar, G. C. Thomas, and R. D. Gregg, "Optimally biomimetic passivity-based control of a lower-limb exoskeleton over the primary activities of daily life," *IEEE Open J. Control Syst.*, vol. 1, pp. 15–28, 2022.

[28] R. Ortega, A. Van Der Schaft, B. Maschke, and G. Escobar, "Interconnection and damping assignment passivity-based control of port-controlled hamiltonian systems," *Automatica*, vol. 38, no. 4, pp. 585–596, 2002.

[29] R. Ortega, A. J. Van Der Schaft, I. Mareels, and B. Maschke, "Putting energy back in control," *IEEE Control Syst. Mag.*, vol. 21, no. 2, pp. 18–33, 2001.

[30] J. Pratt, C.-M. Chew, A. Torres, P. Dilworth, and G. Pratt, "Virtual model control: An intuitive approach for bipedal locomotion," *The International Journal of Robotics Research*, vol. 20, no. 2, pp. 129–143, 2001.

[31] G. Lv, H. Xing, J. Lin, R. D. Gregg, and C. G. Atkeson, "A task-invariant learning framework of lower-limb exoskeletons for assisting human locomotion," in *American Control Conf.* IEEE, 2020, pp. 569–576.

[32] J. Camargo, A. Ramanathan, W. Flanagan, and A. Young, "A comprehensive, open-source dataset of lower limb biomechanics in multiple conditions of stairs, ramps, and level-ground ambulation and transitions," *J. Biomech.*, vol. 119, p. 110320, 2021.

[33] N. Divekar, J. Lin, C. Nesler, S. Borboa, and R. D. Gregg, "A potential energy shaping controller with ground reaction force feedback for a multi-activity knee-ankle exoskeleton," in *IEEE Int. Conf. Biomed. Robot. Biomechatron.*, 2020.

[34] H. K. Khalil, *Nonlinear systems*. Upper Saddle River, NJ: Prentice Hall, 2002, vol. 3.

[35] D. J. Braun and M. Goldfarb, "A control approach for actuated dynamic walking in biped robots," *IEEE Trans. Robot.*, vol. 25, no. 6, pp. 1292–1303, 2009.

[36] M. Grant and S. Boyd, "CVX: Matlab software for disciplined convex programming, version 2.1," http://cvxr.com/cvx, Mar. 2014.

[37] B. Laschowski, R. S. Razavian, and J. McPhee, "Simulation of stand-to-sit biomechanics for design of lower-limb exoskeletons and prostheses with energy regeneration," *bioRxiv*, p. 801258, 2020.

[38] IEE Smart Sensing Solutions, "Smart footwear: Sensing solutions for medical & sports," https://iee-sensing.com/health-tech/medical-sports/smart-footwear-sensing-solutions/, 2022.

[39] J. F. Yang and D. Winter, "Electromyographic amplitude normalization methods: improving their sensitivity as diagnostic tools in gait analysis." *Arch. Phys. Med. Rehabil.*, vol. 65, no. 9, pp. 517–521, 1984.

[40] D. D. Molinaro, I. Kang, J. Camargo, M. C. Gombolay, and A. J. Young, "Subject-independent, biological hip moment estimation during multimodal overground ambulation using deep learning," *IEEE Trans. Med. Robot. Bionics*, 2022.

[41] P. J. Millington, B. M. Myklebust, and G. M. Shambes, "Biomechanical analysis of the sit-to-stand motion in elderly persons," *Arch. Phys. Med. Rehabil.*, vol. 73, no. 7, pp. 609–617, 1992.

[42] T. Lenzi, M. C. Carrozza, and S. K. Agrawal, "Powered hip exoskeletons can reduce the user's hip and ankle muscle activations during walking," *IEEE Trans. Neural Syst. Rehabil. Eng.*, vol. 21, no. 6, pp. 938–948, 2013.